This document is confidential and is proprietary to the American Chemical Society and its authors. Do not copy or disclose without written permission. If you have received this item in error, notify the sender and delete all copies.

Enhanced dimensional accuracy of material extrusion 3D printed plastics through filament architecture

Journal:	ACS Applied Polymer Materials
Manuscript ID	ap-2021-00110p.R2
Manuscript Type:	Article
Date Submitted by the Author:	n/a
Complete List of Authors:	Ai, Jia-Ruey; The Pennsylvania State University - University Park Campus, Chemical Engineering Peng, Fang; The University of Akron, Polymer Engineering Joo, Piljae; The University of Akron, Polymer Engineering Vogt, Bryan; Pennsylvania State University, Chemical Engineering

SCHOLARONE™ Manuscripts

Enhanced dimensional accuracy of material extrusion 3D printed plastics through filament architecture

Jia-Ruey Ai, 1,2 Fang Peng, 2 Piljae Joo, 2 and Bryan D. Vogt 1,*

¹Department of Chemical Engineering, The Pennsylvania State
University, University Park, PA 16802, United States

²Department of Polymer Engineering, University of Akron, Akron,
OH 44325, United States

ABSTRACT: Optimization of 3D print conditions for material extrusion of plastics by fused filament fabrication typically involves trade-offs between mechanical properties and dimensional accuracy due to their orthogonal requirements. Increased polymer mobility improves the mechanical properties by chain diffusion to strengthen the interfaces between printed roads, but flow associated with the high polymer mobility leads to inaccuracies. Here, we describe the application of a model core-shell geometry

in filaments to address these trade-offs and understand the materials requirements to achieve improved dimensional accuracy. Systematic variation of the core with commercial polycarbonatebased plastics when using a common high-density polyethylene shell illustrates that tensile properties obtained with these filaments are relatively insensitive to printing conditions and selection of the core polymer, but the dimensional accuracy of the printed part improves markedly as the glass transition temperature of the core polymer increases. The impact resistance of the core-shell based parts is dependent on the selection of the core polymer with a significant decrease in impact resistance for the lowest modulus core. Although warping can be mostly mitigated with the core-shell filaments, the printed object in general is smaller than the digital source due to large volume change associated with high crystallinity of HDPE. The dimensional accuracy is dependent on the solidification temperature and mechanical properties of the polymers comprising the filament, print conditions, and the local geometry of the object as quantified by layer-by-layer analysis of 3D scanned images of the printed objects. Both processing changes and structures in the digital object that can degrade the dimensional accuracy are identified through this analysis. core-shell filament structure represents a model geometry to understand potential for the printing of polymer blends where separation of solidification temperatures in co-continuous blends could provide a route to improve performance.

KEYWORDS: fused filament fabrication; polyethylene; polyolefin; polymer blend; fused deposition modeling (FDM^{TM})

INTRODUCTION

The transition of three-dimensional (3D) printing from prototyping¹ to additive manufacturing (AM)² has been realized through improvements in machine design.³ process control and optimization,⁴ and feedstock materials⁵ to produce parts with properties adequate for use in products. AM enables highly customized manufacturing with personalization and topology designs that are not achievable in conventional manufacturing, but the properties of 3D printed parts are typically dependent on the processing details, particularly for material extrusion (MatEx) printing of plastics.^{6, 7} This 3D printing method, which includes fused filament fabrication (FFF) also known as fused deposition modeling (FDMTM) as trademarked by Stratasys, mimics traditional manufacturing with the ability to produce parts with a variety of high performance engineering thermoplastics.⁸⁻¹⁰ However, the mechanical properties of these 3D printed plastics are typically inferior to those from injection molding with a large variance¹¹ that can challenge efficient design. The poor mechanical properties of 3D printed parts have been attributed to the incomplete development of the interface between printed roads¹² due to limitations of polymer diffusion and incomplete filling of the printed part due to the circular cross-section extrudate from the hot end. 13 Despite these limitations associated with MatEx 3D printing, these printers have been at the forefront of response to supply chain limitations in the response to COVID-19 pandemic. 14, 15 The low-cost and convenience of FFF printers 16 offers many opportunities for AM if process sensitivity, mechanical properties and part-to-part variation can be addressed with lower

cost filaments, particularly polyolefins (ethylene and propylene). Polyolefins dominate traditional manufacture of plastic parts ¹⁷ due to their combination of very low cost and reasonable mechanical properties.

However, polyolefins are challenging to print via MatEx as crystallization tends to generate stresses to delaminate the part during printing.^{18, 19} For high density polyethylene (HDPE), modification of the build plate with a thermoplastics elastomer improves the adhesion of the part by relieving some stresses to generate parts that visually resemble the desired part.¹⁹ Alternatively, a large brim increases the adhesion to the build plate for MatEx printing of HDPE.²⁰ Additionally, the dimensional accuracy can be improved by manipulating the crystallization stresses through blending with other polymers to decrease the total volume change,²¹⁻²³ additives to alter the crystallization,²⁴ or inclusion of filler reinforcements.^{25, 26} The use of polymer blends represents potentially the simplest route, but the requirements of the blend to obtain the required dimensional accuracy and mechanical properties are not clear.

The transient nature of the 3D printing process with MatEx produces a distribution of thermal history through the printed part. This thermal history is generally key for the development of the interface that controls mechanical properties. Typically, this history is optimized for the mechanical properties, ^{27, 28} but the optimization tends to neglect considerations for dimensional accuracy of complex objects consistent with products. The temperature history along with the rheology of the polymers during the print²⁹ should define the stress development that can cause warpage and deformation.³⁰

Here we systematically examine the influence of core polymer chemistry, through a series of polycarbonates (PC), in core-shell filaments with a common HDPE shell to understand the polymer properties that control both mechanical properties and dimensional accuracy of the 3D

printed parts. The core-shell architecture for the filaments based on coextrusion provide a model filament system where the morphology is essentially invariant to understand polymer blends in 3D printing. This is critical as blend morphology can dramatically influence the mechanical properties. A simple concentric structure is used for the coextruded filaments, but more complex geometries are possible.31 PC-based materials were selected on the basis of (1) 3D printed PC exhibits reasonable mechanical properties and dimensional accuracy^{32, 33} and (2) the availability of commercial PC based materials with variation in thermal properties to enable a systematic investigation without completely altering the chemistry. Traditional manufacturing (e.g., compression molding) with PC provides high toughness parts,³⁴ but 3D printing of PC via MatEx tends to lead to significant reduction in the strength and toughness of PC parts.³⁵⁻³⁷ One route to improve their mechanical properties is inclusion of continuous carbon fibers.³⁸ Here, the core material can act similar to these continuous fibers to reinforce the HDPE matrix. Additionally, sample warping can be mitigated as the T_g of core increases, which we attribute to mechanical reinforcement by the glassy PC during crystallization of the HDPE. The dimensional accuracy of the Benchy boat structure illustrates how print path history can exasperate the effects of the core polymer selection. A layer-by-layer mean square error approach is demonstrated to provide a route to quantify differences in dimensional accuracy. These results illustrate the importance of separation of thermal transitions in multiple component polymer systems for MatEx to provide enhanced dimensional accuracy for complex parts.

EXPERIMENTAL SECTION

Material Feedstock and their Characterization. Nitrogen (high purity > 99.998%) was purchased from Praxair. The molecular mass and its distribution for the different polymers were

determined from size exclusion chromatography (Figure S1). Bisphenol-A polycarbonate (PC, Makrolon 3208, M_n = 31790 g/mol, D = 1.71), a proprietary polycarbonate copolymer (cPC, APEC 1797, M_n = 22960 g/mol, D = 1.96), and PC-ABS blend (PC-ABS, Bayblend T45PG, M_n = 29900 g/mol, D = 2.52) were obtained from Covestro AG. High density polyethylene (HDPE, SunTec B161 M_n = 6660 g/mol, D = 215) was obtained from Sun Chemical. Note that the large dispersity is associated with a multimodal distribution that contains a low (M_n = 908 g/mol, D = 1.18) and high (M_n = 40530 g/mol, D = 40) mass molecular component. All molecular masses are reported relative to polystyrene standards. These commercial polymers were used to fabricate core-shell filaments for 3D printing.

Prior any processing, the polymer pellets were dried under vacuum (-30 in. Hg) for > 12 h to remove residual moisture. The temperature used for drying was polymer dependent: cPC, 130 °C; PC,120 °C; PC-ABS, 100 °C; and HDPE, 80 °C. Note that this drying step is critical for the polycarbonates as residual moisture leads to polymer degradation.³⁹ The thermal properties of the resins were assessed by differential scanning calorimetry (DSC, TA Instruments Q200). The DSC experiments were performed at 10°C min⁻¹ in hermetically sealed aluminum pans (DSC Consumables, Inc.) under nitrogen atmosphere. This rate was selected as it is commonly used to assess transitions in polymers. The thermograms from DSC were recorded on cooling from 240 °C after being held for 10 min at 240 °C to eliminate the thermal history. 4.0 to 6.0 mg of polymer from the virgin pellets was used for each DSC experiment. The solidification of the printed part occurs on cooling and these DSC thermograms provides some insights into stresses that can deform the printed structure. The thermograms on subsequent heating were used to determine the temperature floor for the processing and print extrusion temperatures.

3D Printing. Two single-screw extruders (HAAKE, Rheomix 252p and Akron Extruder M-PAK 150) were connected through a custom circular opening co-extrusion die (diameter = 2 mm) as described previously⁴⁰ to fabricate the core-shell filaments. Details about the filament fabrication are included in the supporting information (SI). The composition of the filaments was quantified by optical micrographs of filament cross-sections as described in the SI. Fig. S2 illustrates optical micrographs of the core-shell filaments. The core fraction was calculated from the area ratio of the core to that of the entire filament using ImageJ.⁴¹ All filament diameters were measured along their length with calipers and the average diameter for each filament was used in the software for control of the extrudate during printing. Prior to printing, the filaments were dried under vacuum (-30 in. Hg) at 80 °C for >12 h. Higher temperatures for drying led to fusion of the filaments due to surface melting of the HDPE. Nonetheless, drying of the filaments is critical with the use of polycarbonates in the core as these can degrade at high temperatures when water is present.⁴²

For all printed objects, the build surface was covered by an AddicoreTM Kapton (polyimide) film and coated at 120 °C with a thin layer of a poly (vinyl alcohol) adhesive (Elmer's glue stick) just prior printing. This surface provides sufficient adhesion with the printed polymers examined to avoid failure of the print due to delamination, but the adhesion is sufficiently low for removal without requiring a raft. One object was printed at a time to provide a consistent process history for each part. The g-codes were generated from the object models with Simplify3D (version 4.1.1).

An open-source 3D printer, Cartesio W0.9, equipped with a 1.75 mm type E3D-V6 hot-end, modified E3D cartridge heater 24V – 40W and 0.4 mm nozzle was used to print objects for mechanical testing with the core-shell filaments. Both standard impact bars (ASTM-D256) and tensile bars (ASTM-D638V) were printed with 0.25 mm layer height, 20 mm/s printing speed, 100

% infill, 0°/90° infill pattern, cooling fan turn off and extrusion temperatures from 260 °C to 320 °C. Fig. S3 illustrates the print orientation (xy) of both the impact and tensile bars used in this study. The impact bar was printed as a solid rectangular object and then notched post printing to provide the appropriate precrack for the impact test.

A standard object used to assess the limits of printability, "3DBenchy Boat", ^{19, 43} was printed using the core-shell filaments with a German RepRap X500 equipped with a 0.4 mm nozzle. All boats were printed using the following conditions: 0.25 mm layer height, 50 mm/s printing speed, 10 % infill, 0°/90° pattern and an extrusion temperature of 320 °C. The cooling fan on the extruder was not active until after the 14th layer to prevent warping in the first few layers. For subsequent layers, the cooling fan was operated at full speed. This change in the fan operation was standard from the software. The two printers used for the different shapes were selected simply for convenience associated with the availability of the printers at the time. Both printers were capable of printing all of the specimens examined.

Mechanical Testing. The mechanical properties of the 3D printed parts were directly measured from parts printed to match the size of standard Type IV injection molded specimens. The tensile properties were determined using protocols associated with ASTM D638V using an Instron 5567 with a load cell of 1000 N. The specimens were printed to the specification of Type IV tensile bars with a gauge length of 25 mm. The specimens were stretched at 10 mm/min until failure. All measurements were performed at room temperature. The thickness and width of the test specimens were measured with digital caliper (Husky® 1467H) prior to the tensile test to calculate the engineering stress. The Young's modulus, strain at break and fracture toughness were all determined from the stress-strain curves that were tested in triplicate for each print condition.

Higher rate impact tests were performed using the Izod impact resistance test (ASTM D-256). The specimens were printed to the same dimensions as injection molded impact bars and a 2.54 mm notch was cut using a standard notch cutter (Model TMI 22-05, Testing Machine Inc.). The impact resistance was measured using an Instron Ceast 9050 with 5.5 J pendulum energy with three specimens at each condition tested for statistics.

Quantifying Shape and Microstructure. The internal structure associated with the core-shell structure of the printed parts was elucidated with X-ray microcomputed tomography (μ CT, GE v|tome|x L300 multi-scale nano/ μ CT system). The μ CT scanner operated at 50 kV/200 μ A without a filter and X-ray images were recorded every 0.4° over a range of 180°. The electron density differences between the core and the shell polymers provided sufficient contrast for μ CT to be directly visualized the core and shell separately. The impact and tensile bars after failure were examined with μ CT to understand the failure mechanisms.

To quantify the dimensional accuracy of the printed 3D benchy boats, optical 3D reconstructions were produced using a blue light scanning camera (Polyga, HDI-C109) equipped with a rotatory stage. The 3DBenchy boats were painted with white paint (RUST-OLEUM White Primer). The images were captured using the FlexScan3D software (Polyga, version 3.3.12). Prior to scanning, the camera system was calibrated with a rotary calibrating board, following the standard scanning procedure from the manufacturer. The accuracy is reported to be 35 μm. The full structure reconstruction, including surface topography, used multiple scans of each side of the printed part (front, back, two sides, top and bottom) when the face was directly facing the camera. The object was fixed by non-hardening model clay (Sargent Art®) on the rotatory stage. Images were captured every 30° over the full 360°. The series of images from each scan were analyzed

through mesh generation to generate partial 3D images. The dimensional accuracy was quantified with GOM Inspect 2019 by direct comparison of the mesh model obtained from the 3D scan with the original digital model used in the print by the 3-point alignment method. Details of the analysis method are included in the SI.

RESULTS AND DISCUSSION

The core-shell filaments were produced by coextrusion as shown schematically in Figure 1. The PC-based (cPC, PC, PC-ABS) core materials and HDPE shell materials were melt processed separately at temperatures that were suggested by the manufacturer prior to being joined in a coextrusion die. The relative flow rates were regulated by melt pumps to control the composition to a target of 50 vol%. The effective flow rates for the melt pumps were set by the melt pump speed of 20 rpm (identical for each). The extruded core-shell filaments were quenched in a temperature-controlled water bath and wound using a take-up wheel whose velocity was marginally greater than the extrusion rate to provide tension on the filament. The drawdown slightly decreases the filament diameter from the die diameter (1.75 mm) to 1.75 ± 0.017 mm, 1.71 ± 0.020 mm, and 1.67 ± 0.015 mm for cPC, PC, and PC-ABS core filaments, respectively. Fig. S2 shows the optical images of the cross-section to determine the filament compositions: 47.5%, 47.9%, and 43.5% for cPC, PC, and PC-ABS, respectively, in the core-shell filaments.

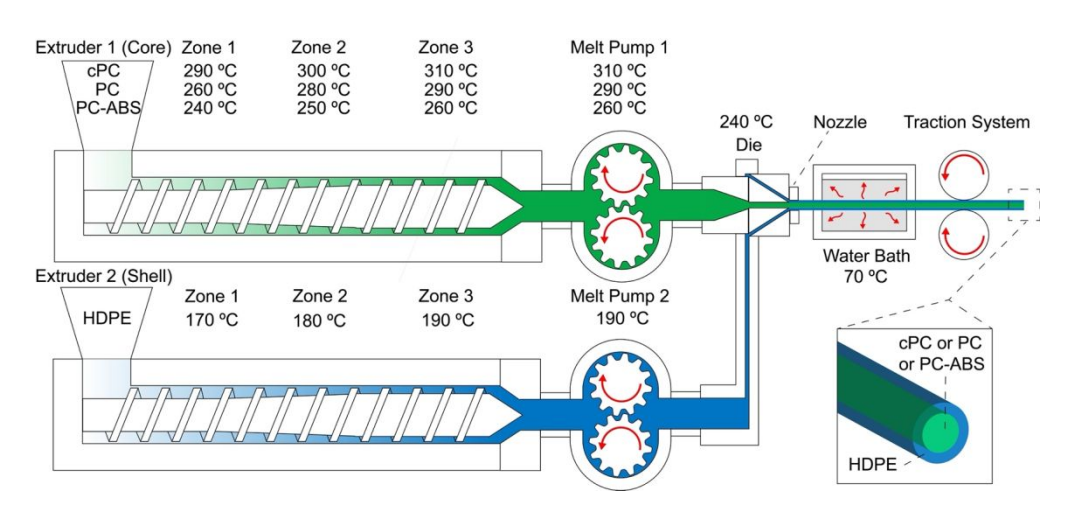


Figure 1. Schematic of co-extrusion system and parameters for the production of core-shell filaments. In the schematic, the core materials (cPC, PC or PC-ABS) are shown in green, while the shell material (HDPE) is shown in blue.

For printing the core-shell filaments, the thermal extrusion process remains unchanged from standard filament MatEx printing processes. The extruder temperature of the 3D printer must exceed both critical flow temperature (T_{cf}) for amorphous core and melting temperature (T_{m}) of semicrystalline shell.⁴⁴ To understand the lower temperature processing limits associated with 3D printing of the core-shell filaments, the thermal properties of the individual polymers were measured by DSC as shown in Figure 2 with a peak at $T_{c} = 117^{\circ}$ C from the crystallization of the HDPE, while a kink in the thermograms for the PC materials is associated with the glass transition. It should be noted that the rate of cooling (10° C/min) is orders of magnitude slower than typically encountered during printing,⁴⁵ but the cooling rates comparable to that observed in 3D printing cannot be achieved with a conventional DSC. From the thermograms, T_{c} provides guidance for the build platform temperature, which was set to 120° C to minimize crystallization of the first several printed layers to prevent delamination / warpage. Figure S4 illustrate the DSC themogram on heating, which illustrates the T_{m} (136° C) and temperature floor for melt processing HDPE. From Figure 2, the glass transition temperature (T_{g}) of core materials is 163° C (cPC), 143° C (PC) and

 124°C / 99°C (PC-ABS). Due to limited miscibility of PC and ABS at the composition of this commercial blend, two glass transitions are observed. For polymer processing, temperatures > T_g are necessary, typically 50-100 °C greater than T_g , and the minimum processing temperature defines T_{cf} . At extrusion temperatures below 260°C with these filaments, the extrudate is inconsistent and the surface finish is poor as shown in Figure S5.

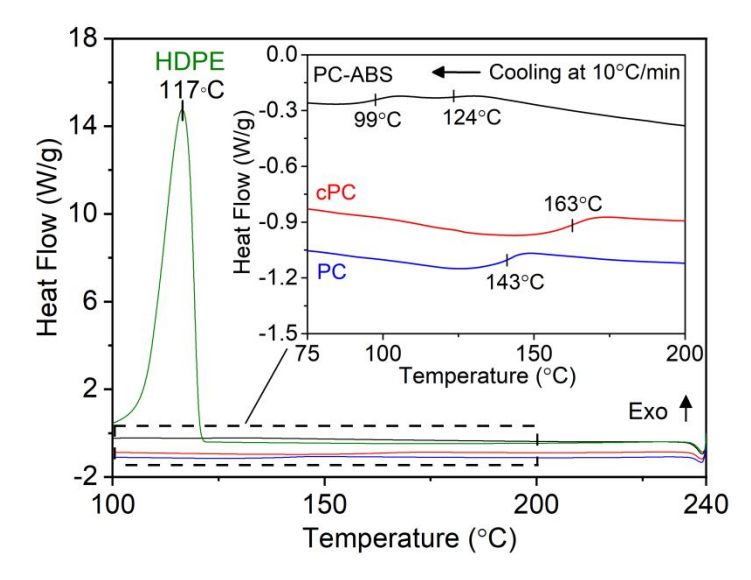


Figure 2. DSC thermograms on cooling at 10° C/min for each of the individual polymers used in the filaments. The polymers were first heated to 240° C and held for 10 min to remove thermal history prior to cooling. The exotherm from crystallization of HDPE (green) dominates the heat flow. The inset shows the kinks in the thermograms associated with the glass transition temperature (T_g) of PC, cPC and PC-ABS. The crystallization temperature and T_g are noted on the thermograms for the different polymers.

This poor printability of cPC and PC core-shell filament at lower temperatures is attributed to the mismatched viscosity and elasticity of the polymer melt. A viscosity ratio for the core:shell close to unity is stable, but flow instabilities will occur as the mismatch grows.⁴⁷ The differences in the temperature dependence of the viscosity for the PC-based materials in the glass forming region⁴⁸ and the HDPE melt lead to an increasing disparity in the viscosities of the core and shell

plastics as T_g is approached. The lower T_g of the PC-ABS leads to a lower viscosity mismatch at 240°C and less inconsistency in the extrusion during printing (Figure S5). The high temperature limit is set by the polymer decomposition temperature. The initial decomposition temperature (IDT) of HDPE, PC and ABS are 410°C, 450°C, and 340°C, respectively. ^{42, 49, 50} The lowest IDT provides an upper limit for comparisons between the different core materials. Thus, extrusion temperatures between 260 and 320 °C were examined.

Figure 3 illustrates the printed objects from the three different core-shell filaments at a constant extrusion temperature of 280 °C. Figure 3A illustrates the printability of the filaments using a common test object in the maker community, a Benchy boat. Differences in the part quality can be resolved visually with the cPC core leading to a better-quality print. However, the complexity of the boat part makes it challenging to quantify the differences in the quality. Typically, warping or bending measurements on simple bars are used to assess potential for deformation and the printability of filaments. 18 Figure 3 illustrates the warping of the impact bars printed under the same conditions. The impact bar printed with the highest T_g core, cPC, is nearly flat (Figure 3B) with a radius of curvature of approximately 70 mm. With PC as the core material (Figure 3C), the impact bar is clearly not as flat. The curvature of the sample becomes more extreme with the PC-ABS core (Figure 3D) with an average radius of curvature of 28 mm in this case. The radius of curvature for these printed impact bars are shown in Figure S6A. The warping of the printed bars results from stresses associated with the non-isothermal MatEx printing. ³⁰ During printing, stress is mitigated in the melt state, but will accumulate on cooling below the solidification temperatures (e.g., T_{g} or T_{c}) to lead to warping and deformation of the printed object.³⁰

In the case of multicomponent filaments, the core material solidifies at a temperature greater than the HDPE shell (T_g > T_c), so the core is floating in a melt of HDPE to prevent transfer of the stresses associated with contraction of the core material from Tg to Tc of the HPDE.21 At temperatures well above T_c of HDPE, the melt will dissipate stresses through viscous losses.³⁰ However when the printed part is cooled locally to $\leq T_c$, the HDPE will decrease its volume by crystallization, but the glassy core will resist bending. Figure S7 illustrates that the crystallinity of the printed parts is independent of the core polymer selection, so the efficacy in maintaining the shape with these core-shell materials is directly related to core material properties as the relative composition of the filaments and the shell material are the same across the filaments. In particular, resistance to bending should be directly related to the elastic modulus of the core polymer. Cooling through T_g leads to an appreciable increase in elastic modulus over a narrow temperature window. With T_g of PC-ABS close to T_c for the HDPE, the low modulus of PC-ABS at T_c allows for substantial deformation of the printed bar (Figure 3D). Although the reported moduli at ambient temperature are similar for the 3 core polymers, the 20 °C difference in Tg between cPC and PC should effectively provide a significant difference in the quench depth into the glass at T_c of the HDPE. The observed curvature (Figure 3E) is consistent with these arguments associated with the difference between T_c and T_g driving the mechanics of the reinforcement by the core polymer.

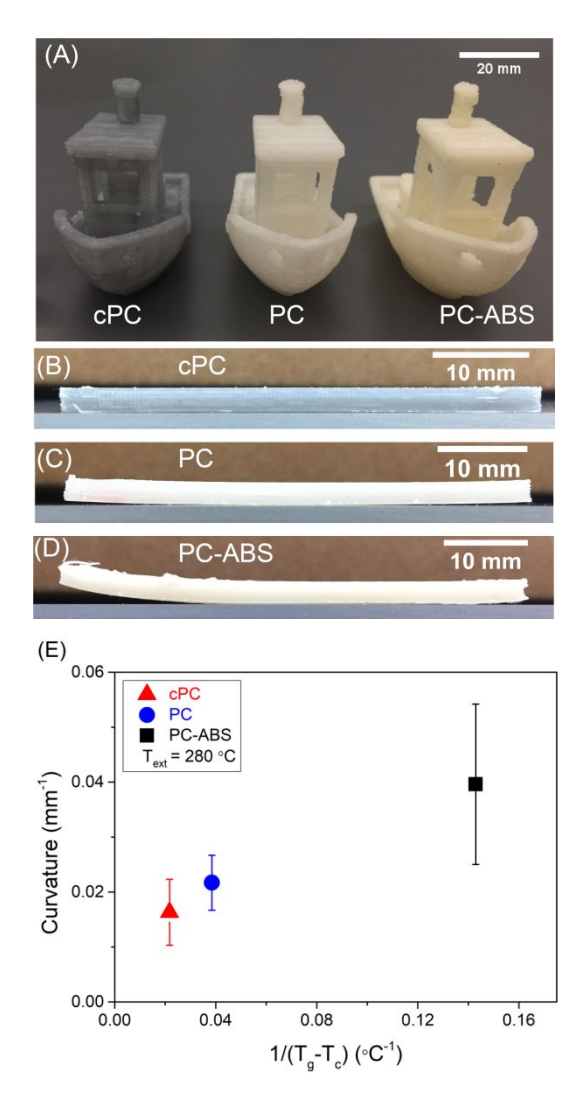


Figure 3. (A) Photograph illustrating the 3D benchy boat printed with the core-shell filaments as labeled by the core material. Side view of impact bars printed at T_{ext} = 280°C with T_{bed} = 120°C with cores of (B) cPC, (C) PC and (D) PC-ABS. (E) The bending curvature scales inversely with T_g of the core polymer. The average of three specimens with its standard deviation ($\pm \sigma$) are presented.

The warp deformation of the impact bars provides a clear indicator of the improved dimensional accuracy of the cPC core in these filaments f, but how this translates to complex objects for products is not clear. To address this, Benchy boats (Figure 3A) are used to provide a methodology to provide a more quantitative description of the dimensional accuracy. Figure 4

illustrates the 3D accuracy maps based on the difference between the digitalized dimensions of printed Benchy boats and the digital design. Most of the deviations are associated with insufficient material as the actual dimensions are smaller than the digital model. Smaller size due to contraction on crystallization is a common problem with semicrystalline polymers and generally the digital design is modified to correct for the contraction. Due to the referencing of the printed object to the model, the port side is always reported as smaller than the digital model (Figure 4A). Examination of the front of the boats (Figure 4A) illustrates that there is a challenge in printing the bow where the object comes to a point and the top of the pipe. The inclined structure of the high-chin spoon bow requires printing with unsupported overhang, but there are other layers with similar overhang that do not exhibit as large of a deviation. The deviation in the bow of the boat and in the pipe region (Figure 4B) is magnified with the PC core in comparison to the cPC core. Although printing of objects with only HDPE requires modifications to minimize warp delamination,²¹ the Benchy boat printed with the cPC alone exhibits similar dimensional accuracy (Figure S8) to the cPC-HDPE core-shell filament when printed under identical conditions. However, the Benchy boat printed with cPC alone has a crack through the hull region (Figure S8) due to stresses developed during printing and the brittle nature of the 3D printed cPC.

Visually, even with the color maps, differences between the PC and cPC core materials in dimensional accuracy for the printing of the Benchy boats with core-shell filaments are not great in other regions. Visually for these two filaments, the difference in the warpage of the impact bars (Figure 3C and 3D) is substantially greater than the dimensional accuracy differences in the Benchy boat (Figure 4). The deviations with the boats printed with core shell filaments using an PC-ABS core are much greater. The pipe region is particularly problematic with the PC-ABS core filament, although the smaller posts and the roof of the cabin also exhibit relatively poor shape

accuracy with the PC-ABS core (Figure 4C). We attribute this performance to the accumulation of heat during printing of small areas and the lower solidification temperature of the PC-ABS.

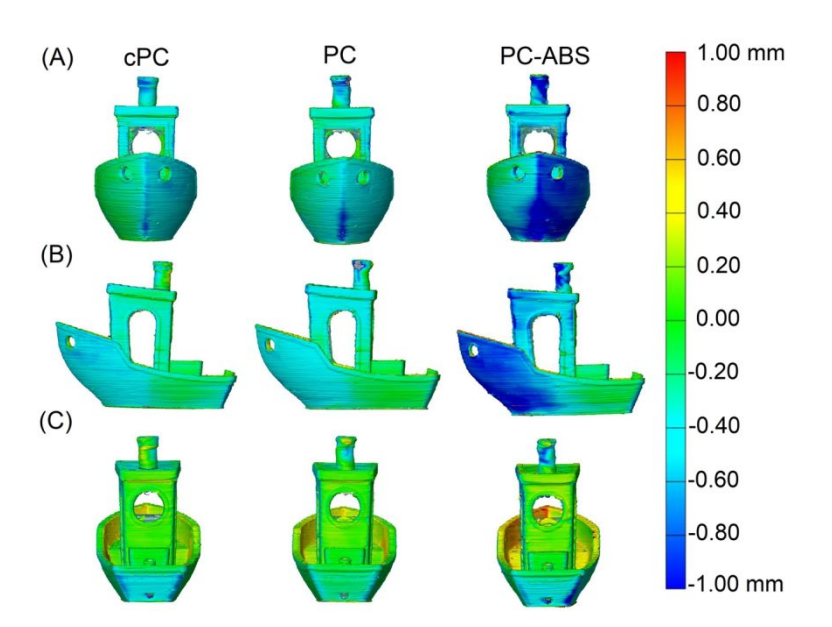


Figure 4. False color 3D scan images illustrating the deviation from the model for 3D benchy boats for the 3 core-shell filaments with (A) front, (B) side and (C) back view. Consistent print parameters were used for all boats: $T_{\text{ext}} = 320^{\circ}\text{C}$, printing speed 50 mm/s and layer thickness 0.25 mm. Regions in green indicates the printed object (as represented by the local point cloud fit) deviates less than \pm 0.2mm from the model. Red areas are protruded relative to the model.

The localization of defects in certain layers for the printed Benchy boats for the different filaments suggests that some features may be more sensitive to the characteristics of the filaments. Understanding these effects could be helpful for validation and certification for manufacturing. The false color mapping of the object is qualitatively insightful (Figure 4), but does not allow for direct quantitative comparisons. Warp deformation is simply defined by the radius of curvature,³⁰ but this only applies to simple print geometries. To quantify the dimensional accuracy performance

for these Benchy boats, a mean square error analysis was adapted to each individual building layer. Within each layer, there are n voxels and the deviation from the digital model is known for each voxel $(x_i - \hat{x}_i)$. Utilizing this information, the mean square error (MSE) for each layer was calculated as:

$$MSE = \frac{1}{n} \sum_{i=1}^{n} (x_i - \hat{x}_i)^2$$

By applying this analysis to each printed layer of the Benchy boat, the average error associated with each layer can be quantified and compared as shown in Figure 5. These data can illustrate the print paths and processing conditions that lead to problems with dimensional accuracy. Tool path during the print is known to influence the printing process and the ultimate properties.⁵¹ The average dimensional accuracy with the PC and cPC cores is similar in comparison to the higher MSE obtained in almost all cases with the PC-ABS core. The voxel by voxel deviations for several of the layers are shown in Figure S9. Some layers show only negative deviations from the digital model, while others exhibit a combination of positive and negative deviations. It should be noted that the deviation from the model contains contributions from both the filaments and intrinsic variations associated with the printer operations. Figure S10 illustrates the variation in the MSE for a replicate print with the cPC core-shell filaments. The differences in the MSE between the prints tends to be smaller than the differences with the variation in core-shell filaments shown in Figure 5. The general features in terms of minima and maxima in the MSE are generally observed in both prints.

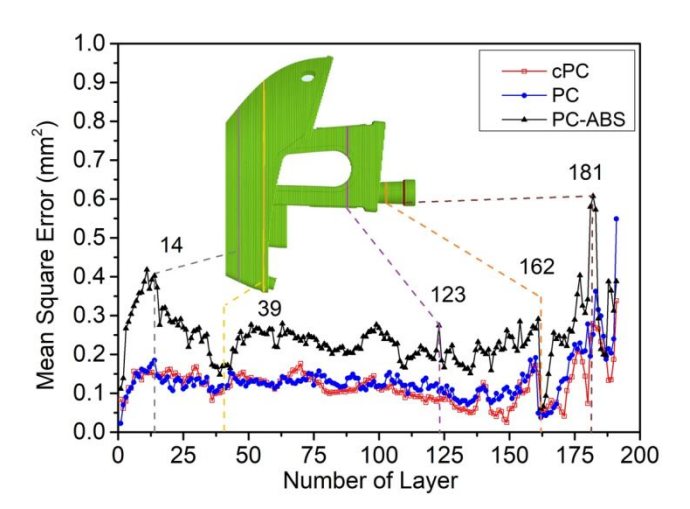


Figure 5. Layer-based quantification of the dimensional accuracy from the mean square error analysis for the printed boats.

Examination of the MSE for the better performing PC and cPC core containing materials illustrates general correlations in the MSE between layers with aperiodic peaks (Fig. 5). The location of these peaks match in some cases for all three filaments suggesting a design or process feature that tends to promote inaccuracies in the print, which are associated with the 3D printer performance and the tool path. The changes in MSE can in general be explained by the localization of heating, asymmetries in stresses due to overhang and differences in the print path of the adjacent layers, and the T_g of the filament core. At layer 14, the cooling fan on the extruder is activated, which increases the cooling rate to decrease the deformation of the printed structure. Layer 39 is close to where the lower hull is completed and the combination of less overhang and smaller print area in subsequent layers improves the dimensional accuracy. The unsupported print to generate the window occurs at layer 124, where sag in the printed road leads to a spike in the MSE at layer 123. This sag in the print can be observed visually for the PC-ABS core material (Figure S11). Localization of heating and the poor thermal conductivity of the polymer leads to changes in the dimensional accuracy of the pipe region at the top of the boat (layers 162 and 181). A more detailed discussion on the differences in the MSE is included in the SI.

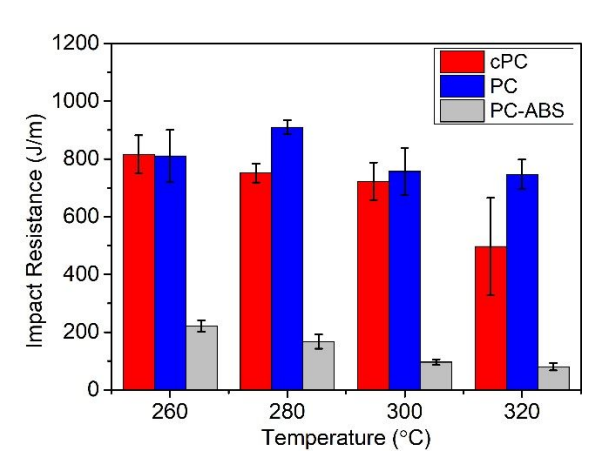


Figure 6. Role of selection of core material and extrusion temperature on the impact resistance of printed parts using core-shell filaments. The impact resistance using cPC and PC cores is significantly greater than that for the PC-ABS core. All results reported are the average of three specimens with standard deviation ($\pm \sigma$).

Beyond dimensional accuracy, the mechanical properties of the printed objects in AM are critical to their utility for most applications. Fig. 6 shows the influence of the core chemistry and extrusion temperature (260°C to 320°C) on the impact resistance. The data from these impact tests are shown in Table S1. For reference, the impact resistance for PC and PC-ABS is reported to be 600 J/m and 320 J/m, respectively, for injection molded materials.^{52, 53} When these polymers are printed using MatEx, an impact resistance of only 45 J/m and 150 J/m for PC and PC-ABS, respectively, is reported.^{21, 40} This reduction in mechanical properties for the 3D printed parts is generally attributed to weak weld lines and embedded air gaps between printed roads.⁵⁴ Although injection molded HDPE exhibits lower impact resistance (115 J/m) than these core materials,⁵⁵ the impact resistance of samples printed with core-shell filament is greater than that of injection molded PC in some cases (Fig. 6), which is attributed to additional energy dissipation mechanisms associated with the composite structure. As shown in Fig. 6, the impact resistance of the parts printed with PC-ABS core are significantly lower than observed for the other core-shell filaments.

The decrease in impact resistance with increasing print temperature for the PC-ABS/HDPE coreshell materials could be associated with the morphology of PC-ABS blend.⁵⁶ The string and bead structure of the dispersed PC phase tends to transition to a quasi-continuous structure at higher temperatures, which deteriorates their mechanical properties.⁵⁶

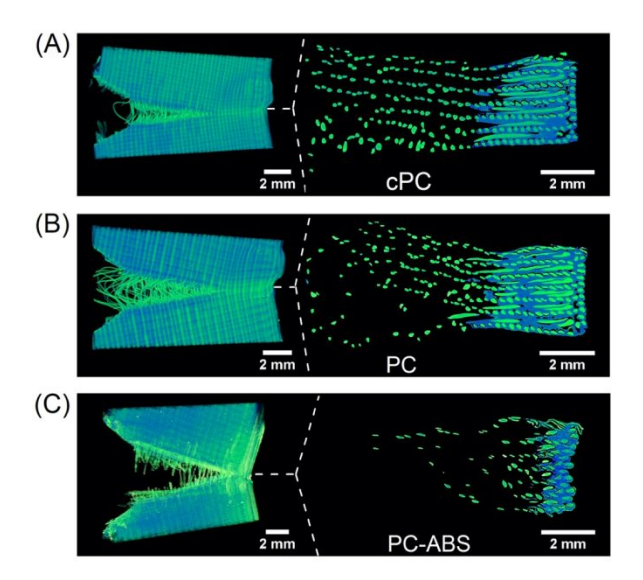


Figure 7. X-ray μ CT reconstructed images of impact bars printed at T_{ext} = 280°C after impact testing for core-shell prints with (A) cPC, (B) PC, and (C) PC-ABS cores. The higher electron density core is shown in green color (cPC, PC and PC-ABS), while the blue corresponds to the HDPE material. A side view of the 3D reconstructed images is showed on the left, while a cross-section through the center of the notch region is on the right.

In order to understand the differences in impact resistance, the structure near the failure was examined using x-ray tomography (Figure 7). There is sufficient x-ray contrast to visualize the core and shell to enable the volume fraction of the core polymer to be determined in the printed part. The core polymer was found to comprise 46.8 vol%, 47.2 vol% and 42.6 vol% of the printed polymer for cPC, PC, and PC-ABS, respectively, which are all slightly less than original filament

compositions determined optically (Fig. S2). Mismatch of viscosity between polymer melts can causes the instability at interface,⁵⁷ but the mismatch can also alter the annular co-flow⁵⁸ to change the composition of core-shell extrudate. In this case, the less viscous shell develops a greater velocity than the more viscous core, which leads to a decrease in the overall core composition. The differences in viscosity of the core and shell were sufficient to slightly alter the composition, but not so large to deteriorate the core-shell architecture that would occur in the case of flow instabilities.

To explain the impact data in Figure 6, an additional energy dissipation mechanism must be present in the core-shell printed materials to provide the observed toughness. Figure 7A illustrates that the crack propagates from the cut precrack through the HDPE, but fibers of the cPC core bridge the crack. Examination of micrographs illustrate some voids forming at the interface between the cPC and HDPE. These voids are distinct from voids that are formed during the print. Examination of the x-ray tomography images away from the deformation zone provides quantification of the void fraction in the printed parts to be: 2.68% (cPC/HDPE), 2.81% (PC/HDPE), and 0.06% (PC-ABS/HDPE). These void fractions are significantly less than that for parts printed with PC⁴⁰ or PC-ABS²¹ alone, but also illustrate how solidification of the core can act to limit large scale flow. The voids formed during deformation provide an energy dissipation mechanism through the energy required to form a new surface, which increases toughness.⁵⁹ The stretching of the glassy core fiber with pull-out at core-shell interface slide and dissipate impact energy through frictional toughening⁶⁰ or cavitation from the mechanical mismatch between the core and shell could provide the mechanism for the void formation. The frictional toughening will depend on the mismatch in the coefficient of thermal expansion (CTE) of the core and shell through

the crystallization-induced shrinkage of the HDPE around the core fiber, where stress from HDPE crystallize would increase the frictional force.⁶¹ These energy dissipation mechanisms, which require two phases, are consistent with the observed impact resistance of these printed parts that exceeds that of the individual components (Fig. 6). Similar structures are observed with the PC core material as shown in Figure 7B, but the width of the crack is increased with the PC core and some PC fibers break across the interface near the notch to provide additional energy dissipation.

Printing with the PC-ABS core leads to substantially lower impact resistance (Fig. 6). As shown in Fig. 7C, most of the PC-ABS fibers bridging the crack have fractured and the crack has extended further into the specimen. The void fraction decreased, as shown in Figure S12, to reduce one energy dissipation mechanism, but this change in void fraction is similar to the difference between cPC and PC. This suggests that cavitation is not primarily responsible for the improved toughness of the objects printed with core-shell filaments. The competition between frictional resistance and inherent mechanical properties of PC-ABS provides one explanation for the much lower impact resistance. Core fibers oriented perpendicularly to the impact experience uniaxial tension as the pendulum strikes impact bar. The fiber pull-out mechanism requires individual fiber to withstand the applied load to dissipate the energy at interface through frictional toughening. The ultimate stress of PC-ABS is hypothesized to be less than the load required to dissipate energy through frictional resistance. Thus, the printed core shell objects containing PC-ABS dissipate drastically less energy and allow the crack to propagate further into the specimen. These features are common to the samples after impact as shown in Figure S13.

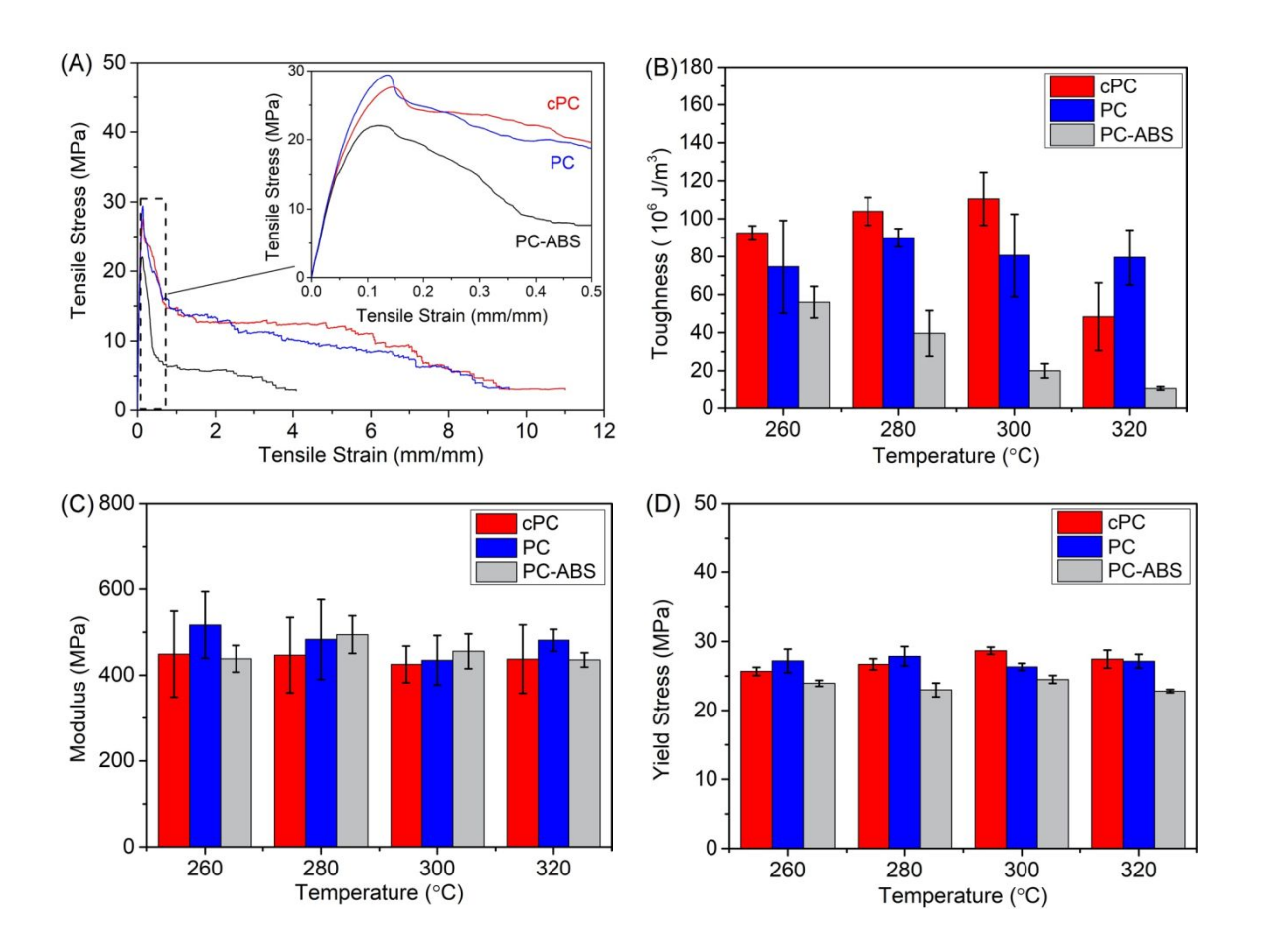


Figure 8. (A) Representative tensile stress-strain curves for the 3D printed core-shell materials. The tensile bar specimens were printed at $T_{\text{ext}} = 280 \,^{\circ}\text{C}$, printing speed 20 mm/s and 0.25 mm layer thickness. The yielding behavior is associated with the failure of the HDPE with fibers of the core holding the specimen. (B) Toughness determined from the area under stress - strain curve. From the tensile data, the core selection or extrusion temperature have a limited effect on the (C) elastic modulus and (D) yield stress for the core-shell printed tensile bars. In all cases, three specimens were tested, and the properties reported are the average with the standard deviation ($\pm \sigma$).

Figure 8 illustrates the tensile properties of the samples printed at 280 °C. The stress-strain curves for the other extrusion temperatures examined are shown in Figure S14. The stress-strain curves illustrate the fiber reinforcement by the core materials with multiple yielding steps at

progressively higher strain. These step decreases in the stress are associated with the failure of individual core fibers that are bridging the crack that forms in the HDPE phase. The elastic modulus (inset in Figure 8A) is similar between the different cores when printed at 280 °C, but the yield stress is lower for the PC-ABS core materials. The toughness from low rate tensile measurements do not necessarily always follow qualitative trends from toughness associated with high rate impact tests.⁶³ The toughness determined from the area under the stress strain curve prior to failure (Figure 8B) are qualitatively consistent with the impact properties. The differences in toughness between the two mechanical tests is also consistent with the frictional toughening. Additional discussion about the toughness is available in the SI. X-ray tomography imaging illustrates the formation of voids during the tensile deformation as well as shown in Figure S15.

Figure 8C illustrates that the elastic moduli are nearly independent of print extrusion temperature and the core material selection. The matrix material is HDPE in all cases, while the core material acts as fiber reinforcement when printed in the direction of the applied strain. The modulus of the materials should be described by composite theory,⁶⁴ but the relative modulus of the materials printed with PC-ABS core is greater than expected based on their intrinsic mechanical properties. This difference could be influenced by the interfacial properties between the core and shell, similar to the importance of the interfaces for fiber composites,⁶⁵ as there are apparent differences in the energy dissipation mechanisms from the impact measurements. Figure 8D illustrates that the yield stress for the printed tensile bars is also relatively insensitive to the extrusion temperature, but consistently lower for PC-ABS as expected. The relatively small influence of printing conditions on the mechanical properties with the core-shell could be

beneficial for manufacture as this suggests the potential for a broader process operation window for the print to achieve consistent properties.

The tensile properties associated with printing of the core shell materials can be directly compared with printed core materials alone. Figure S16 shows the stress-strain curve for cPC, while the tensile data for 3D printed PC⁴⁰ and PC-ABS²¹ have been previously reported Table S2 summarizes the mechanical properties to illustrate the differences between the core-shell and single polymer filaments. The addition of HDPE as expected decreases the elastic modulus of the core-shell printed parts in comparison to the printed PC, cPC or PC-ABS alone. However, there is a significant increase in the ductility with the core-shell filaments. While 3D printed PC or cPC is extremely brittle, the PC-ABS exhibits some stress whitening during the tensile test, but the strain after yielding is still limited in comparison to the core-shell materials. It is interesting to note that PC-ABS is phase separated with a string-bead structure, ⁵⁶ so the more ductile printed parts are all associated with multiphase materials.

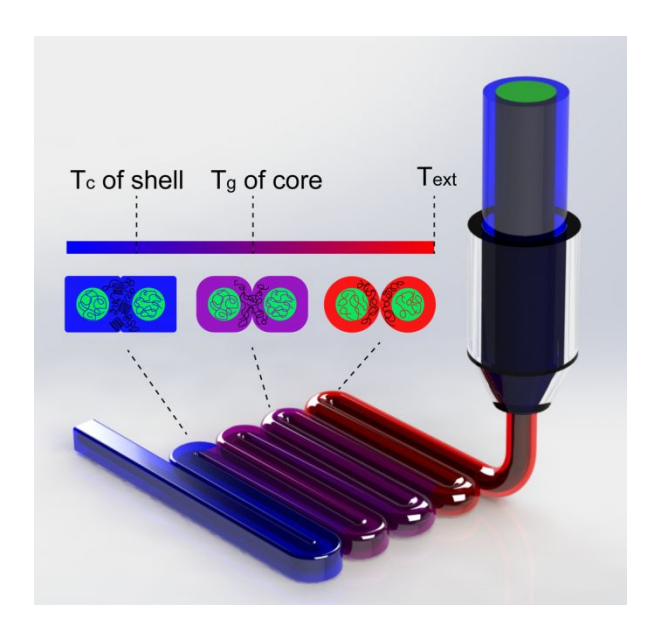


Figure 9. Schematic illustrating the proposed mechanisms associated with the printability of the core-shell filaments. As the extrudate cools, three stages are proposed that define the final printed structure. (i) both core and shell are in the melt state that allows flow to fill large voids locally. (ii) The extrudate cools sufficiently fast to the T_g of the core polymer to prevent large scale flow, while shell remain a melt for further interfacial development between printed roads. (iii) The extrudate cools to T_c where the HDPE crystallizes around the solidified core fibers that acts reinforcement to prevent warpage.

To explain the results for mechanical properties and dimensional accuracy associated with the core-shell filaments, a mechanism is proposed based on diffusion/flow, separation of solidification, crystallization and composite bending. As shown Figure 7, the extruded filaments retain the core-shell structure to produce printed roads with HDPE on its exterior. crystallization of the HDPE across the interface provides a locking mechanism for mechanical strength as shown schematically in Figure 9. This crystallization reduces the requirements of polymer chain diffusion across adjacent extruded lines to effectively bond the material in comparison to typical glassy polymers used in MatEx.66 The interface development between printed roads is assisted by the T_c of HDPE being lower than the T_g of the core materials. The core materials can be accurately printed at higher extrusion temperatures to enable increased time for flow of the HDPE shell to improve the fill of the part by removing voids between printed roads, while the solidification of the core polymer limits the scale of the flow. Initially as printed, both the core and shell polymers are in the melt, but cooling will lead to a solid fiber floating in a HDPE melt. This solid component provides reinforcement similar to long fiber composites. The mitigation of voids and crystallization between the roads likely contributes to the ductile fracture of the parts printed with these core-shell filaments. The composite structure provides additional

potential mechanisms for energy dissipation (e.g., fiber pull-out at interface, cavitation, plastic deformation of the fibers) that are commonly not present in 3D printed plastic parts. The results suggest that friction associated with fiber pull-out is primarily responsible for the increased impact resistance of the parts printed with the core-shell filaments. Additionally, minimization of voids within the part decreases the potential stress concentrators that propagate cracks. For filaments based on polymer blends, these ideas can also apply where added mobility of one phase can reduce the voids and crystallization of one phase can improve the interfacial strength between printed roads to improve the mechanical properties.

From the perspective of dimensional accuracy, one of the challenges with HDPE is its fast crystallization rate and high crystallinity that produce rapid and substantial volume shrinkage.⁶⁷ This crystallization can even be problematic for conventional injection molding processes if the cycle time and temperature are not appropriately selected.⁶⁸ The non-crystalline core material reduces the total volume of crystalline material to decrease the total stress applied and acts as reinforcement in a manner similar to long fiber composites. Printing HDPE alone requires additional mitigation steps such as a large brim²⁰ or modified print platform surface.¹⁹

Although the results reported are limited to HDPE (shell) – polycarbonates (core), the systematic variation in the thermal properties of the core polymer can provide insights into other potential systems. For example, polyethylene terephthalate (PET) has less warpage issues than HDPE when 3D printed and exhibits excellent mechanical properties,²² which could lead to improved dimensional accuracy as a shell material. High temperature liquid crystal polymers provide enhancements in the mechanical properties,⁶⁹ but a core-shell architecture including a semicrystalline shell would enhance the weld strength in the printed part. Similarly, these results

can be applied to polymer blends where one phase solidifies at significantly higher temperatures, which may help to explain some reports about improvements in printing with polymer blends.⁷⁰

CONCLUSIONS

In this work, we demonstrate how engineering of filaments through a core-shell architecture can be used to reduce the trade-offs between mechanical properties and dimensional accuracy in MatEx 3D printing through the selection of the components to maximize the difference in the solidification temperature between the core and shell plastics using a series of commercial polycarbonates and its blend with ABS for the core and a common high density polyethylene (HDPE) shell. The solidification of the core acts to reinforce the printed object by reducing bulk flow and resisting bending to improve the dimensional accuracy. A significantly lower solidification temperature for the shell provides increased mobility between printed roads to strengthen the interfaces and improve the mechanical properties. All of the parts exhibit ductile failure with tensile failure similar to long fiber reinforced composites. Interestingly, the tensile properties from the printed core-shell filaments are not strongly dependent on the extrusion temperature, which suggests that these filaments will produce parts less sensitive to process variation. Moreover, the core-shell architecture increases the impact resistance and toughness of the printed parts; this improvement is associated with energy dissipation from fiber pull-out at the interfaces and plastic deformation of the core materials. Beyond mechanical properties, we illustrated a methodology to assess local changes in the dimensional accuracy for a common complex object, Benchy Boat, from analysis of 3D scanned images. These illustrated that the dimensional accuracy can be strongly dependent on the process history and the geometry of the part with less sensitivity to parts printed with core-shell filaments with the highest T_g core. These

concepts can be applied beyond the core-shell architecture and provide insights into selection of plastic pairs for blends and the desired morphologies of polymer blends for filaments used in MatEx to advance the performance of plastics in additive manufacture.

ASSOCIATED CONTENT

Supporting Information. The following file is available free of charge. Additional experimental protocols, filament cross-sections, DSC thermograms, images and characterization of printed impact bars, local deviations in dimensions between print and digital source, raw impact data, void fraction analysis, tensile stress-strain curves (PDF)

AUTHOR INFORMATION

Corresponding Author

*To whom correspondence should be addressed: bdv5051@psu.edu

ACKNOWLEDGMENTS

This work was financially supported by the National Science Foundation through grants CMMI- 2011289 and CMMI-1825276. The authors appreciate the material support from Covestro LLC (Pittsburgh, PA) for all polycarbonate relative raw materials and Asashi Kasei for high-density polyethylene. We thank Prof Michael A. Hickner for access to the German RepRap x500 3D printer and his group members for training on this printer. The authors thank Siyuan Li, Sierra Yost, James Eagan and Christian Pester for their assistance with the GPC measurements.

REFERENCES

1. Anitha, R.; Arunachalam, S.; Radhakrishnan, P., Critical parameters influencing the quality of prototypes in fused deposition modelling. *J. Mater. Process. Technol.* **2001,** *118* (1-3), 385-388.

- 2. Campbell, I.; Bourell, D.; Gibson, I., Additive manufacturing: rapid prototyping comes of age. *Rapid Prototyping J.* **2012**, *18* (4), 255-258.
- 3. Gao, W.; Zhang, Y. B.; Ramanujan, D.; Ramani, K.; Chen, Y.; Williams, C. B.; Wang, C. C. L.; Shin, Y. C.; Zhang, S.; Zavattieri, P. D., The status, challenges, and future of additive manufacturing in engineering. *Comput.-Aided Des.* **2015**, *69*, 65-89.
- 4. Vijayaraghavan, V.; Garg, A.; Lam, J. S. L.; Panda, B.; Mahapatra, S. S., Process characterisation of 3D-printed FDM components using improved evolutionary computational approach. *International Journal of Advanced Manufacturing Technology* **2015**, *78* (5-8), 781-793.
- 5. Ligon, S. C.; Liska, R.; Stampfl, J.; Gurr, M.; Mulhaupt, R., Polymers for 3D Printing and Customized Additive Manufacturing. *Chem. Rev.* **2017**, *117* (15), 10212-10290.
- 6. Mohamed, O. A.; Masood, S. H.; Bhowmik, J. L., Optimization of fused deposition modeling process parameters: a review of current research and future prospects. *Adv. Manuf.* **2015,** *3* (1), 42-53.
- 7. Casavola, C.; Cazzato, A.; Moramarco, V.; Pappalettere, C., Orthotropic mechanical properties of fused deposition modelling parts described by classical laminate theory. *Mater. Des.* **2016**, *90*, 453-458.
- 8. Das, A.; Chatham, C. A.; Fallon, J. J.; Zawaski, C. E.; Gilmer, E. L.; Williams, C. B.; Bortner, M. J., Current understanding and challenges in high temperature additive manufacturing of engineering thermoplastic polymers. *Additive Manufacturing* **2020**, *34*.
- 9. Marzola, A.; Mussi, E.; Uccheddu, F., 3D Printed Materials for High Temperature Applications. *Design Tools and Methods in Industrial Engineering, Adm 2019* **2020**, 936-947.
- 10. Valino, A. D.; Dizon, J. R. C.; Espera, A. H.; Chen, Q. Y.; Messman, J.; Advincula, R. C., Advances in 3D printing of thermoplastic polymer composites and nanocomposites. *Progress in Polymer Science* **2019**, *98*, 19.
- 11. Lanzotti, A.; Grasso, M.; Staiano, G.; Martorelli, M., The impact of process parameters on mechanical properties of parts fabricated in PLA with an open-source 3-D printer. *Rapid Prototyping J.* **2015**, *21* (5), 604-617.
- 12. Davis, C. S.; Hillgartner, K. E.; Han, S. H.; Seppala, J. E., Mechanical strength of welding zones produced by polymer extrusion additive manufacturing. *Addit. Manuf.* **2017**, *16*, 162-166.
- 13. Wang, X.; Zhao, L. P.; Fuh, J. Y. H.; Lee, H. P., Effect of Porosity on Mechanical Properties of 3D Printed Polymers: Experiments and Micromechanical Modeling Based on X-ray Computed Tomography Analysis. *Polymers* **2019**, *11* (7), 20.
- 14. Ishack, S.; Lipner, S. R., Applications of 3D Printing Technology to Address COVID-19-Related Supply Shortages. *Am. J. Med.* **2020,** *133* (7), E385-E387.
- 15. Vogt, B. D., A Virtual Issue of Applied Polymer Materials: "3D Printing of Polymers". *ACS Appl. Polym. Mater.* **2020,** *2* (6), 2102-2104.
- 16. Stansbury, J. W.; Idacavage, M. J., 3D printing with polymers: Challenges among expanding options and opportunities. *Dent. Mater.* **2016,** *32* (1), 54-64.
- 17. Geyer, R.; Jambeck, J. R.; Law, K. L., Production, use, and fate of all plastics ever made. *Sci. Adv.* **2017**, *3* (7), 5.
- 18. Spoerk, M.; Holzer, C.; Gonzalez-Gutierrez, J., Material extrusion-based additive manufacturing of polypropylene: A review on how to improve dimensional inaccuracy and warpage. *Journal of Applied Polymer Science* **2020**, *137* (12), 16.

- 19. Schirmeister, C. G.; Hees, T.; Licht, E. H.; Mulhaupt, R., 3D printing of high density polyethylene by fused filament fabrication. *Addit. Manuf.* **2019**, *28*, 152-159.
- 20. Gudadhe, A.; Bachhar, N.; Kumar, A.; Andrade, P.; Kumaraswamy, G., Three-Dimensional Printing with Waste High-Density Polyethylene. *ACS Appl. Polym. Mater.* **2019**, *1* (11), 3157-3164.
- 21. Peng, F.; Jiang, H. W.; Woods, A.; Joo, P.; Amis, E. J.; Zacharia, N. S.; Vogt, B. D., 3D Printing with Core-Shell Filaments Containing High or Low Density Polyethylene Shells. *Acs Applied Polymer Materials* **2019**, *1* (2), 275-285.
- 22. Zander, N. E.; Gillan, M.; Burckhard, Z.; Gardea, F., Recycled polypropylene blends as novel 3D printing materials. *Addit. Manuf.* **2019**, *25*, 122-130.
- 23. Chatham, C. A.; Zawaski, C. E.; Bobbitt, D. C.; Moore, R. B.; Long, T. E.; Williams, C. B., Semi-Crystalline Polymer Blends for Material Extrusion Additive Manufacturing Printability: A Case Study with Poly(ethylene terephthalate) and Polypropylene. *Macromol. Mater. Eng.* **2019**, *304* (5), 11.
- 24. Das, A.; Marnot, A. E. C.; Fallon, J. J.; Martin, S. M.; Joseph, E. G.; Bortner, M. J., Material Extrusion-Based Additive Manufacturing with Blends of Polypropylene and Hydrocarbon Resins. *ACS Appl. Polym. Mater.* **2020**, *2* (2), 911-921.
- 25. Qiao, J.; Li, Y. R.; Li, L. Q., Ultrasound-assisted 3D printing of continuous fiber-reinforced thermoplastic (FRTP) composites. *Additive Manufacturing* **2019**, *30*, 11.
- 26. Spoerk, M.; Savandaiah, C.; Arbeiter, F.; Traxler, G.; Cardon, L.; Holzer, C.; Sapkota, J., Anisotropic properties of oriented short carbon fibre filled polypropylene parts fabricated by extrusion-based additive manufacturing. *Composites Part a-Applied Science and Manufacturing* **2018**, *113*, 95-104.
- 27. Aliheidari, N.; Christ, J.; Tripuraneni, R.; Nadimpalli, S.; Ameli, A., Interlayer adhesion and fracture resistance of polymers printed through melt extrusion additive manufacturing process. *Mater. Des.* **2018**, *156*, 351-361.
- 28. Wang, L.; Gardner, D. J., Effect of fused layer modeling (FLM) processing parameters on impact strength of cellular polypropylene. *Polymer* **2017**, *113*, 74-80.
- 29. Das, A.; Gilmer, E. L.; Biria, S.; Bortner, M. J., Importance of Polymer Rheology on Materials Extrusion Additive Manufacturing: Correlating Process Physics to Print Properties. *ACS Applied Polymer Materials* **2021**, *3* (3), 1218-1249.
- 30. Wang, T. M.; Xi, J. T.; Jin, Y., A model research for prototype warp deformation in the FDM process. *Int. J. Adv. Manuf. Technol.* **2007,** *33* (11-12), 1087-1096.
- 31. Hart, K. R.; Dunn, R. M.; Wetzel, E. D., Tough, Additively Manufactured Structures Fabricated with Dual-Thermoplastic Filaments. *Adv. Eng. Mater.* **2020,** *22* (4), 7.
- 32. Rohde, S.; Cantrell, J.; Jerez, A.; Kroese, C.; Damiani, D.; Gurnani, R.; Disandro, L.; Anton, J.; Young, A.; Steinbach, D.; Ifju, P., Experimental Characterization of the Shear Properties of 3D–Printed ABS and Polycarbonate Parts. *Exp. Mech.* **2018**, *58* (6), 871-884.
- 33. Domingo-Espin, M.; Puigoriol-Forcada, J. M.; Garcia-Granada, A. A.; Lluma, J.; Borros, S.; Reyes, G., Mechanical property characterization and simulation of fused deposition modeling Polycarbonate parts. *Materials & Design* **2015**, *83*, 670-677.
- 34. Parsons, E.; Boyce, M. C.; Parks, D. M., An experimental investigation of the large-strain tensile behavior of neat and rubber-toughened polycarbonate. *Polymer* **2004**, *45* (8), 2665-2684.
- 35. Bartolai, J.; Simpson, T. W.; Xie, R. X., Predicting strength of additively manufactured thermoplastic polymer parts produced using material extrusion. *Rapid Prototyping Journal* **2018**, *24* (2), 321-332.

- 36. Reich, M. J.; Woern, A. L.; Tanikella, N. G.; Pearce, J. M., Mechanical Properties and Applications of Recycled Polycarbonate Particle Material Extrusion-Based Additive Manufacturing. *Materials* **2019**, *12* (10).
- 37. Smith, W. C.; Dean, R. W., Structural characteristics of fused deposition modeling polycarbonate material. *Polym. Test.* **2013**, *32* (8), 1306-1312.
- 38. Jahangir, M. N.; Billah, K. M. M.; Lin, Y.; Roberson, D. A.; Wicker, R. B.; Espalin, D., Reinforcement of material extrusion 3D printed polycarbonate using continuous carbon fiber. *Addit. Manuf.* **2019**, *28*, 354-364.
- 39. McNeill, I. C.; Rincon, A., Degradation Studies Of Some Polyesters And Polycarbonates .8. Bisphenol A Polycarbonate. *Polym. Degrad. Stab.* **1991,** *31* (2), 163-180.
- 40. Peng, F.; Zhao, Z. Y.; Xia, X. H.; Cakmak, M.; Vogt, B. D., Enhanced Impact Resistance of Three-Dimensional-Printed Parts with Structured Filaments. *ACS Appl. Mater. Interfaces* **2018**, *10* (18), 16087-16094.
- 41. Schneider, C. A.; Rasband, W. S.; Eliceiri, K. W., NIH Image to ImageJ: 25 years of image analysis. *Nat. Methods* **2012**, *9* (7), 671-675.
- 42. Jang, B. N.; Wilkie, C. A., A TGA/FTIR and mass spectral study on the thermal degradation of bisphenol A polycarbonate. *Polym. Degrad. Stab.* **2004**, *86* (3), 419-430.
- 43. Maurel, A.; Courty, M.; Fleutot, B.; Tortajada, H.; Prashantha, K.; Armand, M.; Grugeon, S.; Panier, S.; Dupont, L., Highly Loaded Graphite–Polylactic Acid Composite-Based Filaments for Lithium-Ion Battery Three-Dimensional Printing. *Chem. Mater.* **2018**, *30* (21), 7484-7493.
- 44. Han, C. D.; Lee, K. Y.; Wheeler, N. C., Plasticating single-screw extrusion of amorphous polymers: Development of a mathematical model and comparison with experiment. *Polym. Eng. Sci.* **1996**, *36* (10), 1360-1376.
- 45. Seppala, J. E.; Han, S. H.; Hillgartner, K. E.; Davis, C. S.; Migler, K. B., Weld formation during material extrusion additive manufacturing. *Soft Matter* **2017**, *13* (38), 6761-6769.
- 46. Nigam, I.; Nigam, D.; Mathur, G. N., Effect of rubber content of ABS on properties of PC/ABS blends. 1. Rheological, mechanical, and thermal properties. *Polym.-Plast. Technol. Eng.* **2005**, *44* (5), 815-832.
- 47. Joseph, D. D.; Bai, R.; Chen, K. P.; Renardy, Y. Y., Core-annular flows. *Annual Review of Fluid Mechanics* **1997**, *29*, 65-90.
- 48. Stillinger, F. H., A TOPOGRAPHIC VIEW OF SUPERCOOLED LIQUIDS AND GLASS-FORMATION. *Science* **1995**, *267* (5206), 1935-1939.
- 49. Murty, M. V. S.; Grulke, E. A.; Bhattacharyya, D., Influence of metallic additives on thermal degradation and liquefaction of high density polyethylene (HDPE). *Polym. Degrad. Stab.* **1998**, *61* (3), 421-430.
- 50. Suzuki, M.; Wilkie, C. A., The thermal degradation of acrylonitrile-butadiene-styrene terpolymei as studied by TGA/FTIR. *Polym. Degrad. Stab.* **1995,** *47* (2), 217-221.
- 51. Kubalak, J. R.; Wicks, A. L.; Williams, C. B., Deposition path planning for material extrusion using specified orientation fields. *47th Sme North American Manufacturing Research Conference (Namrc 47)* **2019**, *34*, 754-763.
- 52. Covestro Makrolon® 3208.

https://solutions.covestro.com/en/products/makrolon/makrolon-3208_56978414-05123120?SelectedCountry=US (accessed May 24th).

- 53. Covestro Bayblend® T45 PG.
- https://solutions.covestro.com/en/products/bayblend/bayblend-t45-pg_56968524-00009096?SelectedCountry=US (accessed May 24th).
- 54. Dawoud, M.; Taha, I.; Ebeid, S. J., Mechanical behaviour of ABS: An experimental study using FDM and injection moulding techniques. *J. Manuf. Process.* **2016**, *21*, 39-45.
- 55. Blom, H. P.; Teh, J. W.; Rudin, A., IPP/HDPE BLENDS INTERACTIONS AT LOWER HDPE CONTENTS. *J. Appl. Polym. Sci.* **1995**, *58* (6), 995-1006.
- 56. Chaudhry, B. I.; Hage, E.; Pessan, L. A., Effects of processing conditions on the phase morphology of PC/ABS polymer blends. *J. Appl. Polym. Sci.* **1998**, *67* (9), 1605-1613.
- 57. Joseph, D. D.; Renardy, M.; Renardy, Y., INSTABILITY OF THE FLOW OF 2 IMMISCIBLE LIQUIDS WITH DIFFERENT VISCOSITIES IN A PIPE. *Journal of Fluid Mechanics* **1984**, *141* (APR), 309-317.
- Han, C. D., *Multiphase flow in polymer processing*. Academic Press: New York, 1981.
- 59. Wetzel, B.; Rosso, P.; Haupert, F.; Friedrich, K., Epoxy nanocomposites fracture and toughening mechanisms. *Eng. Fract. Mech.* **2006,** *73* (16), 2375-2398.
- 60. Cantwell, W. J.; Morton, J., The impact resistance of composite materials—a review. *Composites* **1991**, *22* (5), 347-362.
- 61. Jeon, J.; Muliana, A.; La Saponara, V., Thermal stress and deformation analyses in fiber reinforced polymer composites undergoing heat conduction and mechanical loading. *Compos. Struct.* **2014**, *111*, 31-44.
- 62. Budiansky, B.; Amazigo, J. C., TOUGHENING BY ALIGNED, FRICTIONALLY CONSTRAINED FIBERS. *J. Mech. Phys. Solids* **1989,** *37* (1), 93-109.
- 63. Chen, B. Q.; Evans, J. R. G., Impact strength of polymer-clay nanocomposites. *Soft Matter* **2009**, *5* (19), 3572-3584.
- 64. Jacquet, E.; Trivaudey, F.; Varchon, D., Calculation of the transverse modulus of a unidirectional composite material and of the modulus of an aggregate. Application of the rule of mixtures. *Compos. Sci. Technol.* **2000,** *60* (3), 345-350.
- 65. Gauthier, R.; Joly, C.; Coupas, A. C.; Gauthier, H.; Escoubes, M., Interfaces in polyolefin/cellulosic fiber composites: Chemical coupling, morphology, correlation with adhesion and aging in moisture. *Polym. Compos.* **1998**, *19* (3), 287-300.
- 66. Bellehumeur, C.; Li, L.; Sun, Q.; Gu, P., Modeling of Bond Formation Between Polymer Filaments in the Fused Deposition Modeling Process. *J. Manuf. Process.* **2004,** *6* (2), 170-178.
- 67. Kamal, M. R.; Chu, E., ISOTHERMAL AND NON-ISOTHERMAL CRYSTALLIZATION OF POLYETHYLENE. *Polymer Engineering and Science* **1983**, *23* (1), 27-31.
- 68. Annicchiarico, D.; Alcock, J. R., Review of Factors that Affect Shrinkage of Molded Part in Injection Molding. *Mater. Manuf. Processes* **2014**, *29* (6), 662-682.
- 69. Quintana, J. L. C.; Redmann, A.; Capote, G. A. M.; Perez-Irizarry, A.; Bechara, A.; Osswald, T. A.; Lakes, R., Viscoelastic properties of fused filament fabrication parts. *Addit. Manuf.* **2019**, *28*, 704-710.
- 70. Rocha, C. R.; Perez, A. R. T.; Roberson, D. A.; Shemelya, C. M.; MacDonald, E.; Wicker, R. B., Novel ABS-based binary and ternary polymer blends for material extrusion 3D printing. *J. Mater. Res.* **2014**, *29* (17), 1859-1866.

For Table of Contents Only

